ACS APPLIED MATERIALS & INTERFACES

Research Article

www.acsami.org

# All-in-One Beaker Method for Large-Scale Production of Metal Oxide Hollow Nanospheres Using Nanoscale Kirkendall Diffusion

Jung Sang Cho and Yun Chan Kang*

Department of Materials Science and Engineering, Korea University, Anam-Dong, Seongbuk-Gu, Seoul 136-713, Republic of Korea

Supporting Information

**ABSTRACT:** A simple and easily scalable process for the formation of metal oxide hollow nanospheres using nanoscale Kirkendall diffusion called the "all-in-one beaker method" is introduced. The $Fe_2O_3$, $SnO_2$, NiO, and $Co_3O_4$ hollow nanospheres are successfully prepared by the all-in-one beaker method. The detailed formation mechanism of aggregate-free hematite hollow nanospheres is studied. Dimethylformamide solution containing Fe acetate, polyacrylonitrile (PAN), and polystyrene (PS) transforms into aggregate-free $Fe_2O_3$ hollow nanospheres. The porous structure formed by the combustion of PS provides a good pathway for the reducing gas. The carbon matrix formed from PAN acts as a barrier, which can prevent the aggregation of metallic Fe nanopowders by surrounding each particle. The Fe−C bulk material formed as an intermediate product transforms into aggregate-free $Fe_2O_3$ hollow nanospheres by the nanoscale Kirkendall diffusion process. The mean size and shell thickness of the hollow $Fe_2O_3$ nanospheres measured from the TEM images are 52 and 9 nm, respectively. The discharge capacities of the $Fe_2O_3$ nanopowders with hollow and dense structures and the bulk material for the 200th cycle at a current density of 0.5 A $g^{-1}$ are 1012, 498, and 637 mA h $g^{-1}$, respectively, and their capacity retentions calculated compared to those in the second cycles are 92, 45, and 59%, respectively. Additionally, $Fe_2O_3$ hollow nanospheres cycled at 1 A $g^{-1}$ after 1000 cycles showed a high discharge capacity of 871 mA h $g^{-1}$ (capacity retention was 80% from the second cycle). The $Fe_2O_3$, $SnO_2$, NiO, and $Co_3O_4$ hollow nanospheres show excellent cycling performances for lithium-ion storage because they have a high contact area with the liquid electrolyte and space for accommodating a huge volume change during cycling.

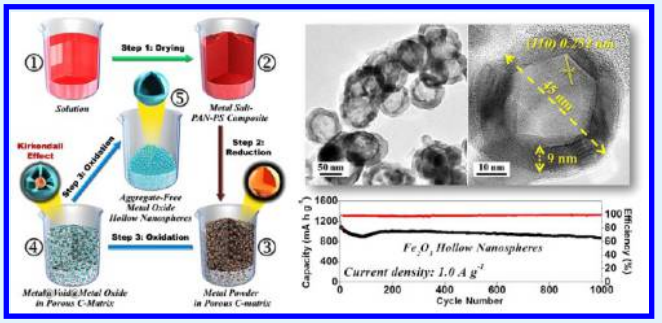


**KEYWORDS:** *Kirkendall diffusion, hollow nanosphere, iron oxide, anode material, lithium-ion battery*

## INTRODUCTION

Hollow nanospheres with controllable size and composition have received great attention because of their distinct morphological advantages over filled nanopowders in diverse applications such as energy storage, solar cells, photocatalysis, gas sensors, and biomedical applications.[1−11] The fabrication of hollow nanospheres generally employs removable templates with a spherical shape and uniform size distribution. Organic polymer and silica nanobeads have been widely used as sacrificial templates because their size and morphology can be easily controlled in laboratory-scale synthesis.[12−18] However, templating methods for hollow nanospheres are usually time-consuming and costly. Therefore, the template-free method employing nanoscale Kirkendall diffusion has received significant attention as a method for producing hollow nanospheres.[2,19−25] In this process, the preparation of aggregate-free metal nanopowders with a dense structure by a well-controlled liquid solution process is an essential requirement. Otherwise, metal nanopowders decorated with carbon-related materials, which are mainly graphene or graphene oxide, are transformed into hollow nanospheres by the nanoscale Kirkendall diffusion process. Recently, Kang et al. reported spherical and nanofiber-type aggregates of hollow nanospheres with various compositions.[23−25] The formation of a carbon matrix embedded with metal nanopowders as an intermediate product was the key idea for the formation of spherical and nanofiber-type aggregates of hollow nanospheres. However, the preparation process of aggregation-free hollow structured nanopowders by using carbon matrix originated form the polymeric precursors has not yet been researched. In addition, in the previous studies, it was essential to utilize the additional equipment of electrospinning or spray pyrolysis process for the preparation of precursor product.[23−25] Therefore, the development of a highly efficient and cost-effective process for large-scale production of hollow nanospheres without a supporting matrix is required in various application fields including energy storage.

In this study, a simple and easily scalable process for metal oxide hollow nanospheres using the nanoscale Kirkendall diffusion process called the "all-in-one beaker method" is introduced. The all-in-one-beaker method does not need

Received: October 27, 2015
Accepted: January 22, 2016
Published: January 22, 2016





DOI: 10.1021/acsami.5b10278
ACS Appl. Mater. Interfaces 2016, 8, 3800−3809

additional equipment for the preparation of the precursor product. The overall process for the preparation of hollow nanospheres was performed sequentially in only one glass beaker in a static furnace. The viscous solution containing the metal salt and organic polymer transformed into aggregate-free metal oxide hollow nanospheres in the glass beaker by a simple drying and thermal treatment process. Transition metal oxide materials has been extensively used in lithium-ion batteries, catalysts, gas sensors, and biomedical applications.[24−35] Therefore, in this study, $Fe_2O_3$, $SnO_2$, NiO, and $Co_3O_4$ hollow nanospheres were selected as the first target materials. The detailed formation mechanism of aggregate-free metal oxide hollow nanospheres by the nanoscale Kirkendall diffusion process using organic polymers as additives was studied. In addition, the electrochemical properties of the metal oxide hollow nanospheres for lithium-ion storage were compared with those of the filled metal oxide nanopowders.

## EXPERIMENTAL SECTION

**Sample Preparation.** Hollow $Fe_2O_3$, NiO, $SnO_2$, and $Co_3O_4$ hollow nanospeheres were synthesized in only one glass beaker in a static furnace via an "all-in-one beaker method." For this, the precursor solution was prepared in a quartz glass beaker by dissolving 5 g of metal salt in 100 mL of *N*,*N*-dimethylformamide (DMF) and adding 5 g of polyacrylonitrile (PAN, $M_w$: 150 000) and 5 g of polystyrene (PS, $M_w$: 192 000) with vigorous stirring overnight. Iron(III) acetylacetonate [$Fe(acac)_3$], nickel(II) acetate tetrahydrate [$Ni(CH_3CO_2)_2(H_2O)_4$], tin(II) 2-ethylhexanoate [$Sn(Oct)_2$], and cobalt(II) acetate tetrahydrate [$Co(CH_3CO_2)_2(H_2O)_4$] were applied as the source materials for $Fe_2O_3$, $SnO_2$, NiO, and $Co_3O_4$, respectively. Then, the glass beaker containing the solution was transferred to the static tube furnace, in which the solution was sequentially post treated in three steps by changing gases. In the first step, the solution was dried for 1 h at 150 °C in air to evaporate the solvent, DMF. Second, the dried powders were reduced at 500 °C for $Fe_2O_3$, NiO, and $Co_3O_4$, and at 400 °C for $SnO_2$ at a heating rate of 5 °C $min^{-1}$ for 3 h under an atmosphere of 10% $H_2$/Ar gas mixture. In the final step, the reduced powders were subsequently oxidized at 400 °C for 3 h identically for all samples at a heating rate of 5 °C $min^{-1}$ in air for the nanoscale Kirkendall diffusion effect to occur, and then were finally cooled down to room temperature. Dense $Fe_2O_3$ nanopowders were also prepared by heat treatment of the dried powders directly at 400 °C for 3 h in air (5 °C $min^{-1}$) without the reduction process as a sample for comparison. Additionally, to investigate the effect of polystyrene (PS) in the above solution, which is expected to form voids in bulk during the process, iron oxide powders were synthesized from a solution without PS by the all-in-one beaker method.

**Characterization.** The microstructures of the metal oxide hollow nanospheres were observed by field-emission scanning electron microscopy (FE-SEM, S-4800, Hitachi) and field-emission transmission electron microscopy (FE-TEM, JEM-2100F, JEOL). In addition, their crystal phases were evaluated by X-ray diffractometry (XRD, X'Pert PRO MPD) using Cu K$\alpha$ radiation ($\lambda$ = 1.5418 Å) at the Korea Basic Science Institute (Daegu). X-ray photoelectron spectroscopy (XPS, Thermo Scientific K-Alpha) with a focused monochromatic Al K$\alpha$ at 12 kV and 20 mA was used to analyze the composition of the specimens. The surface areas of the nanopowders were measured by the Brunauer−Emmett−Teller (BET) method, using $N_2$ as the adsorbate gas. Thermogravimetric analysis was performed using a Pyris 1 TGA (PerkinElmer) over a temperature range of 25−650 °C and at a heating rate of 10 °C $min^{-1}$ under static air atmosphere.

**Electrochemical Measurements.** The electrochemical properties of the $Fe_2O_3$, NiO, $SnO_2$, and $Co_3O_4$ hollow nanospheres were analyzed by constructing a 2032-type coin cell. The anode was prepared by mixing the active material, carbon black, and sodium carboxymethyl cellulose (CMC) in a weight ratio of 7:2:1. Li metal and microporous polypropylene film were used as the counter electrode and the separator, respectively. The electrolyte was 1 M $LiPF_6$ dissolved in a mixture of fluoroethylene carbonate/dimethyl carbonate (FEC/DMC; 1:1 v/v). The discharge/charge characteristics of the samples were investigated by cycling over the 0.001−3.0 V potential range for $Fe_2O_3$, NiO, and $Co_3O_4$ hollow nanopowders and 0.001−1.0 V potential range for $SnO_2$ hollow nanopowders at various current densities. Cyclic voltammograms (CV) were measured at a scan rate of 0.07 mV $s^{-1}$. The dimensions of the anode were 1 cm × 1 cm, and the mass loading was approximately 1.2 mg $cm^{-2}$. The electrochemical impedance was measured using electrochemical impedance spectroscopy (EIS) over the frequency range of 0.01 Hz−100 kHz.

## RESULTS AND DISCUSSION

A schematic of the formation mechanism of the aggregate-free metal oxide hollow nanospheres by the all-in-one beaker method is shown in Scheme 1. Upon drying the dimethylformamide (DMF) solution containing metal salt, polyacrylonitrile

**Scheme 1. (a) Schematic Diagram for the Formation Mechanism of the Aggregate-Free Metal Oxide Hollow Nanospheres by All-in-One Beaker Method and (b) Detail Formation Mechanism of the $Fe_2O_3$ Hollow Nanospheres by Kirkendall Diffusion Effect in a Static Furnace and the Roles of Polystyrene (PS) and Polyacrylonitrile (PAN) Polymers Contained in a Beaker**

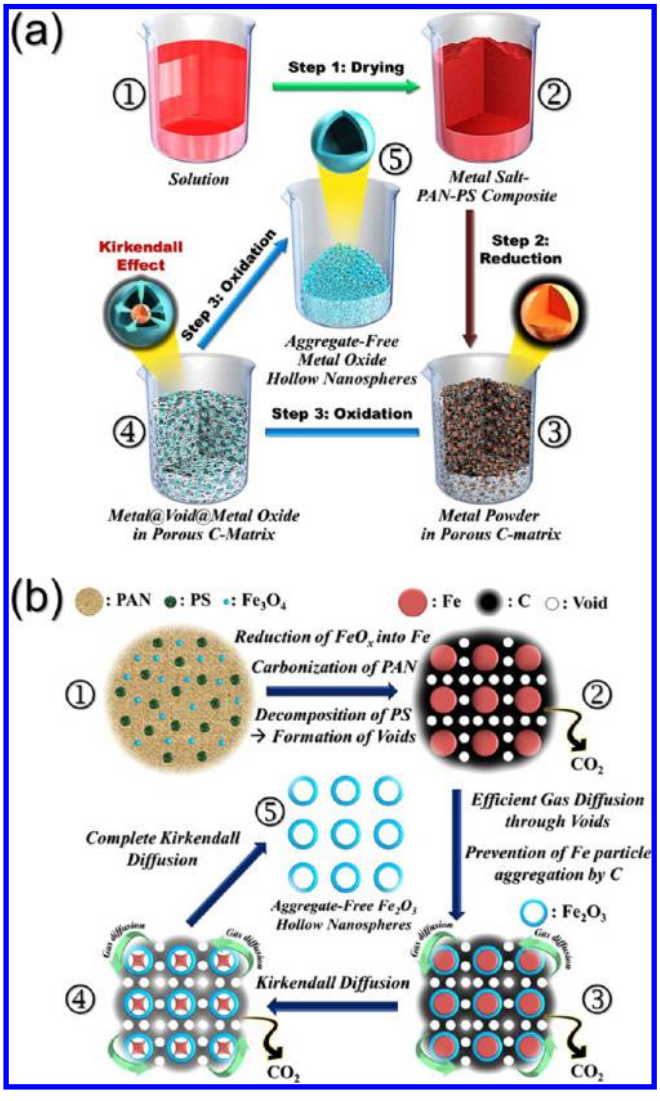




DOI: 10.1021/acsami.5b10278
ACS Appl. Mater. Interfaces 2016, 8, 3800−3809

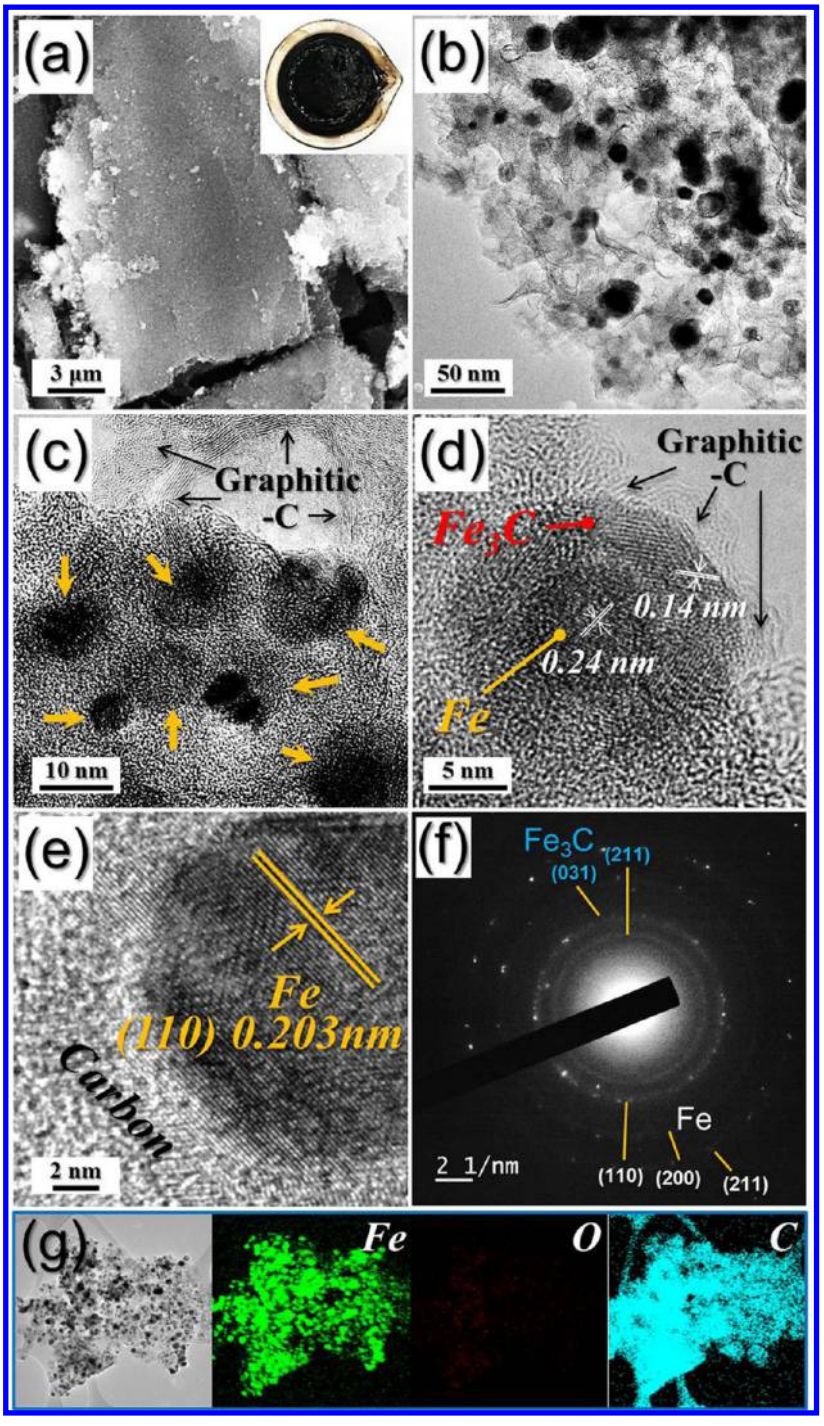


**Figure 1.** Morphologies, SAED pattern, and elemental mapping images of the powders obtained by reduction of the dried precursor powders at 500 °C under 10% $H_2$/Ar gas: (a) SEM image, (b–d) TEM images, (e) HR-TEM image, (f) SAED pattern, and (g) elemental mapping images.

(PAN), and polystyrene (PS) contained in a glass beaker at 150 °C, the metal salt–PVP–PS composite was obtained (Scheme 1a-1,2). Carbonization of PAN during the reduction process produced the bulk carbon matrix (Scheme 1a-2). The complete decomposition and reduction of metal salt into metallic nanopowders occurred during the reduction process under 10% $H_2$/Ar atmosphere (Scheme 1a-3). The complete elimination of PS is achieved by combustion into gases even under a reducing atmosphere (Scheme 1a-3). Therefore, the channels formed by combustion of PS supplied a good pathway for the reducing gas during the Kirkendall diffusion in bulk material (Scheme 1b-2,3,4). Therefore, the metal nanopowders grown uniformly were distributed all over the amorphous carbon matrix during the reduction process. The carbon matrix formed from PAN played the role of a barrier, which can prevent the aggregation of metal nanopowders by surrounding each particle. Thermal treatment of the glass beaker containing the metal-C bulk material under air produced aggregate-free metal oxide hollow nanospheres (Scheme 1a-5). Dense metal nanopowders embedded within the carbon matrix transformed into metal oxide hollow nanospheres by the well-known nanoscale Kirkendall diffusion process.


DOI: 10.1021/acsami.5b10278
ACS Appl. Mater. Interfaces 2016, 8, 3800–3809

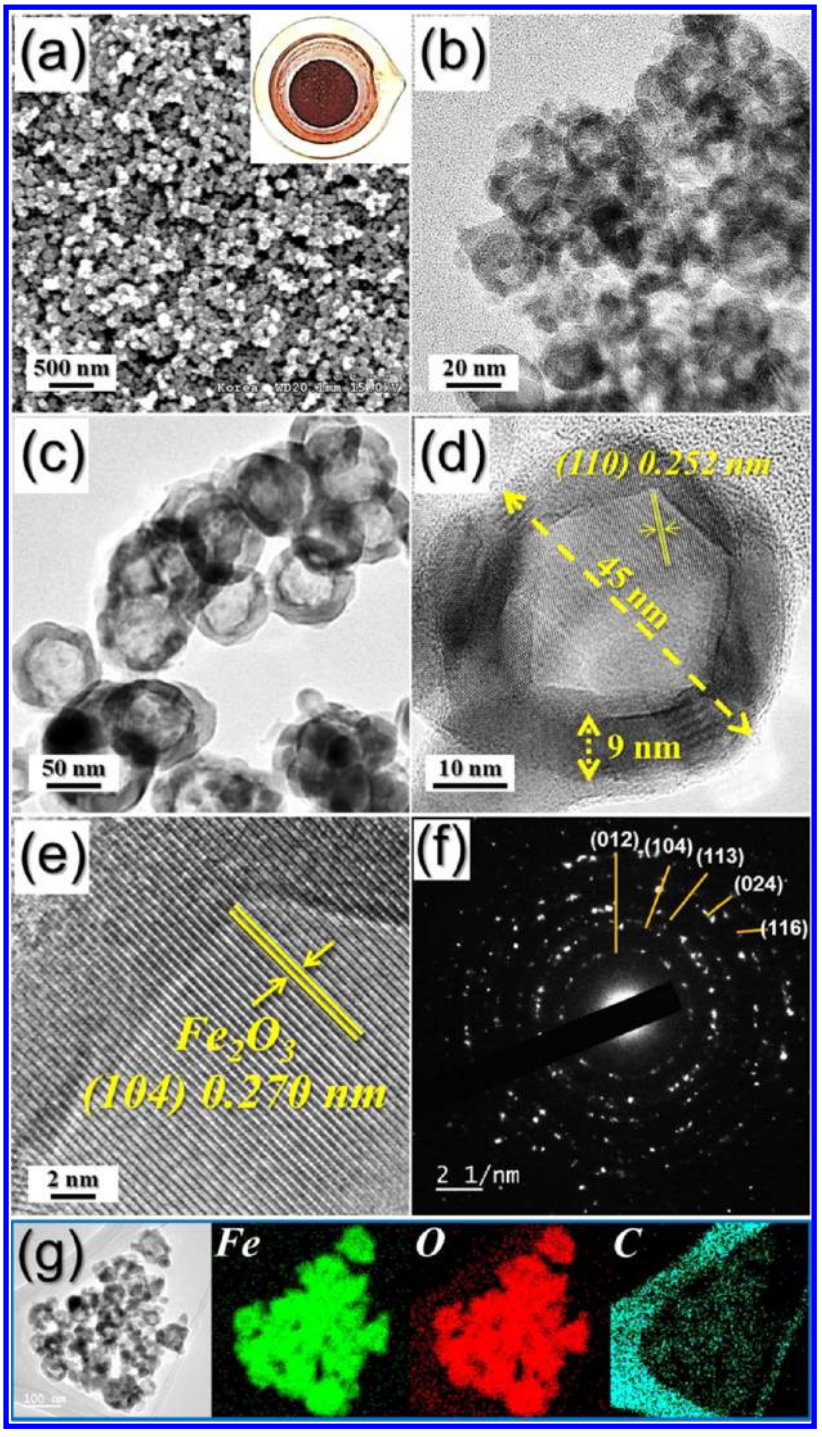


**Figure 2.** Morphologies, SAED pattern, and elemental mapping images of the $Fe_2O_3$ hollow nanospheres formed by all-in-one beaker method: (a) SEM, (b–d) TEM images, (e) HR-TEM image, (f) SAED pattern, and (g) elemental mapping images.

The detailed formation mechanism of the $Fe_2O_3$ hollow nanospheres, which were studied as the main example, is shown in Scheme 1b. Surface oxidation of metallic Fe nanopowder during oxidation resulted in Fe@$Fe_2O_3$ nanopowder with a core–shell structure (Scheme 1b-3). The outward diffusion of the smaller Fe cations ($Fe^{2+}$ = 76 pm, $Fe^{3+}$ = 65 pm) occurred faster than the inward diffusion of oxygen anions ($O^{2-}$ = 140 pm). Accordingly, Kirkendall voids were generated near the Fe/$Fe_2O_3$ interface during vacancy-assisted exchange of the material via bulk interdiffusion (Scheme 1a-4,b-4), which gives rise to coarsening and enhancement of pore growth in the spheres (Scheme 1b-5). Complete conversion of metallic Fe into $Fe_2O_3$ by the nanoscale Kirkendall diffusion process resulted in hollow nanospheres. Combustion of amorphous carbon during the nanoscale Kirkendall diffusion process resulted in the aggregate-free $Fe_2O_3$ hollow nanospheres. In summary, DMF solution containing $Fe(acac)_3$, PAN, and PS transformed into the aggregate-free $Fe_2O_3$ hollow nanospheres by a static three-step post-treatment process inside a glass beaker as described in Supporting Information, Figure S1. The contents of the glass beaker during the preparation of the


DOI: 10.1021/acsami.5b10278
ACS Appl. Mater. Interfaces 2016, 8, 3800–3809

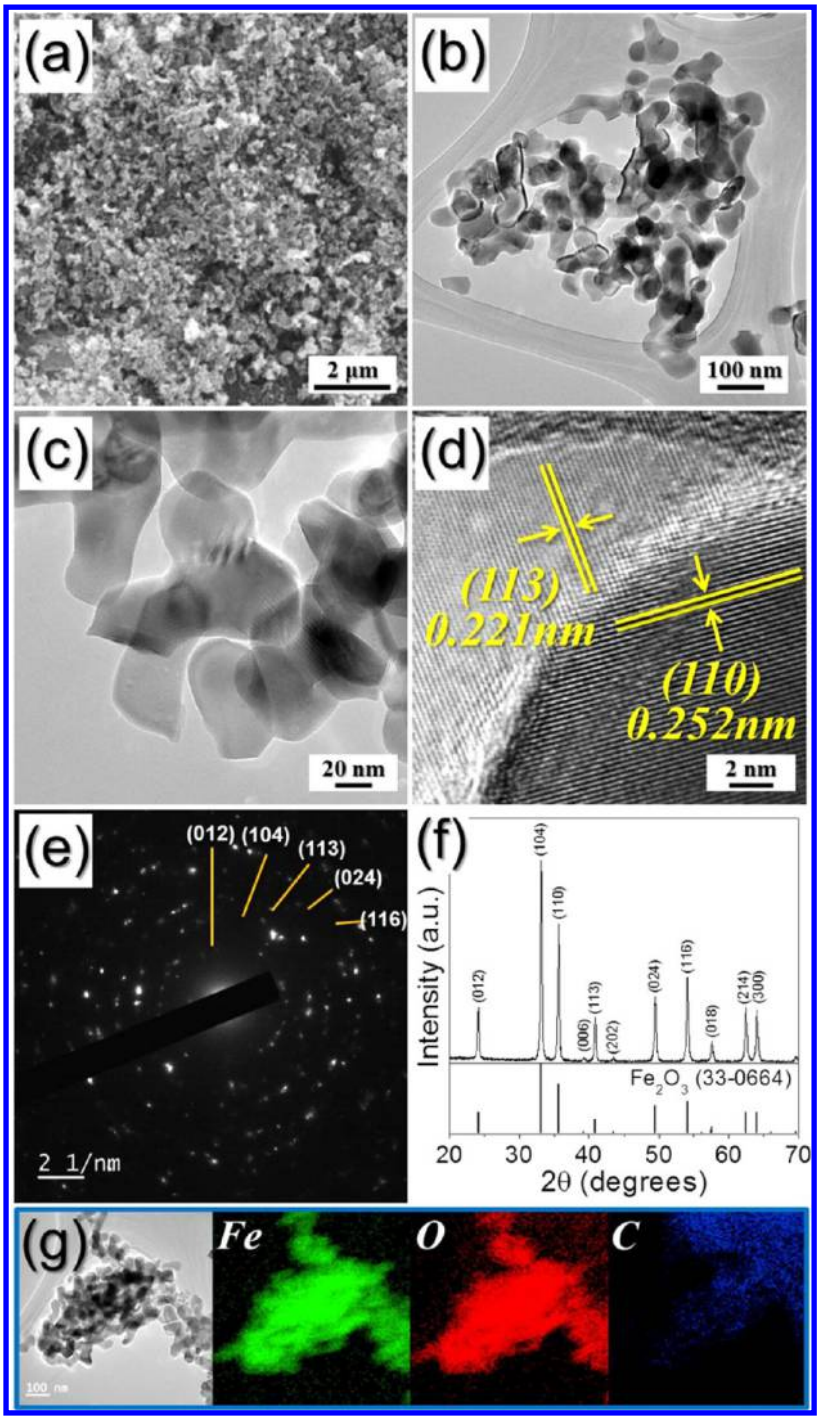


**Figure 3.** Morphologies, SAED pattern, and elemental mapping images of the $Fe_2O_3$ nanopowders with dense structure as a sample for comparison formed by all-in-one beaker method, in which nanoscale Kirkendall diffusion is not applied: (a) SEM, (b,c) TEM images, (d) HR-TEM image, (e) SAED pattern, (f) XRD pattern, and (g) elemental mapping images.

aggregate-free $Fe_2O_3$ hollow nanospheres were not disturbed in any manner.

The formation mechanism of the aggregate-free $Fe_2O_3$ hollow nanospheres by the all-in-one beaker method is investigated based on the morphologies and crystal structures of the materials obtained in each step. The photographs of the beakers containing the product obtained in each step are shown in Supporting Information, Figure S1. The SEM image of the bulk of the sample formed by drying at 150 °C is shown in Supporting Information, Figure S2. The TG curves of PAN and PS obtained in $N_2$ atmosphere are shown in Supporting Information, Figure S3. Decomposition of PAN and PS started at a temperature of 240 and 320 °C, respectively. Therefore, decomposition of PAN and PS did not occur during the drying stage of the solution. The XRD pattern of the dried sample shown in Supporting Information, Figure S4, revealed small peaks of $Fe_3O_4$ formed by partial decomposition of $Fe(acac)_3$. Therefore, the product formed by the drying process was $Fe(acac)_3$−$Fe_3O_4$−PAN−PS composite. The weight loss due to complete carbonization of PAN to form carbon, which occurred below 500 °C under $N_2$ atmosphere, was 58 wt %. On the other hand, PS completely decomposed into gaseous


DOI: 10.1021/acsami.5b10278
ACS Appl. Mater. Interfaces 2016, 8, 3800−3809

products under $N_2$ atmosphere at a temperature of around 400 °C. The TG curve of the product formed by a drying process measured in air showed a three-step weight loss below 500 °C (Supporting Information, Figure S5a) because of the decomposition of $Fe(acac)_3$ into $Fe_2O_3$ and combustion of PAN and PS into gases. From the TG results of PAN and PS, the reduction temperature of the dried material was selected as 500 °C, when amorphous carbon was formed by carbonization of PAN and channels for the hydrogen gas pathway were formed by decomposition of PS. The XRD pattern of the reduced sample at 500 °C had small peaks of metallic Fe and $Fe_3C$, as shown in Supporting Information, Figure S4. Carbonization of metallic Fe to form the $Fe_3C$ layer occurred with amorphous carbon formed by the carbonization of PAN. The broad XRD pattern revealed the ultrafine sizes of the metallic Fe and $Fe_3C$ crystals.

The morphologies of the sample obtained from the beaker after the reduction process is shown in Figure 1. The reduced sample was crushed well by hand due to the complete transformation of the organic polymer into amorphous carbon during the reduction process. The SEM and low-resolution TEM images shown in Figure 1a,b revealed the porous structure of the bulk material. The ultrafine nanopowders with a dense structure are uniformly distributed all over the semitransparent amorphous carbon matrix, as shown in Figure 1b,c. Graphitic carbon formed by the iron catalyst was observed around the Fe nanopowders as shown by arrows in Figure 1c,d. The nanopowder shown in Figure 1d had a clear core−shell structure with the configuration Fe@$Fe_3C$. The TEM image shown in Figure 1d shows lattice fringes separated by 0.14 and 0.24 nm, which correspond to the (200) and (121) crystal planes of metallic Fe and $Fe_3C$, respectively. Carbidation of the surface of the Fe nanopowder formed the core−shell-structured nanopowder. However, the nanopowder shown in Figure 1e had the pure crystalline structure of metallic Fe. The high-resolution TEM image shown in Figure 1e shows clear lattice fringes separated by 0.203 nm, which corresponds to the (110) crystal plane of metallic Fe. The selected area electron diffraction (SAED) pattern shown in Figure 1f revealed the mixed crystalline structure of the Fe and $Fe_3C$ phases. Therefore, some of the Fe nanopowders transformed into the Fe@$Fe_3C$ nanopowders by carbidation during the reduction process. The elemental mapping images shown in Figure 1g showed a trace amount of oxygen and revealed the formation of a carbon matrix with uniform distribution of Fe nanopowders. The TG curve of the product formed by the reduction process measured under air showed a one-step weight loss below 400 °C, as shown in Supporting Information, Figure S5b, because of the combustion of the carbonaceous material formed by carbonization of PAN. The weight loss caused by the combustion of the carbon material was slightly offset by oxidation of Fe and $Fe_3C$.

The product obtained by the reduction process was oxidized at 400 °C under air, as shown in Supporting Information, Figure S1. The bulky black material transformed into a small volume of red-brown colored powders. Combustion of the carbon material and oxidation of the Fe component resulted in $Fe_2O_3$ powders, as confirmed by the color of the product and XRD pattern shown in Supporting Information, Figure S4c. The morphologies of the $Fe_2O_3$ powders formed by the all-in-one beaker method are shown in Figure 2. The SEM and low-resolution TEM images shown in Figure 2a,b revealed the formation of aggregate-free $Fe_2O_3$ hollow nanospheres by the all-in-one beaker method. The TEM images shown in Figure 2b,c revealed the hollow and thin-walled structure of the $Fe_2O_3$ nanospheres. The Fe nanopowders dispersed within the carbon matrix transformed into the hollow $Fe_2O_3$ nanospheres by the nanoscale Kirkendall diffusion process as described in Scheme 1b. The high-resolution TEM images shown in Figure 2d,e revealed a crystalline structure of the hollow $Fe_2O_3$ nanospheres. The high-resolution TEM image showed clear lattice fringes separated by 0.270 and 0.252 nm, which correspond to the (104) and (110) crystal planes of rhombohedral $\alpha$-$Fe_2O_3$, respectively. The SAED pattern shown in Figure 2f also revealed the presence of the phase pure $Fe_2O_3$ nanospheres. The oxidation of Fe into $Fe_2O_3$ is further supported by the Fe 2p XPS spectrum shown in Supporting Information, Figure S6b. There are two peaks at binding energies of 711 eV for Fe $2p_{3/2}$ and 724 eV for Fe $2p_{1/2}$, and a shakeup satellite at 719 eV, which are the characteristic peaks of Fe(III) in $a$-$Fe_2O_3$. No components related to zerovalent Fe and $Fe^{2+}$ are observed.[24−26,30,36] Trace amount of carbon which is graphitic carbon formed by graphitization of amorphous carbon during the reduction process, in which metallic iron acted as catalyst for graphitization was detected in the survey spectrum (Supporting Information, Figure S6a). The elemental mapping images shown in Figure 2g also revealed the presence of carbon in the $Fe_2O_3$ hollow nanospheres. However, the TG curve shown in Supporting Information, Figure S5c revealed the trace amount of carbon in the $Fe_2O_3$ hollow nanospheres. The mean size and shell thickness of the hollow $Fe_2O_3$ nanospheres measured from the TEM images were 52 and 9 nm, respectively. The BET surface area of the hollow $Fe_2O_3$ nanospheres was 21 $m^2$ $g^{-1}$.

The morphologies of the $Fe_2O_3$ nanopowders formed as a sample for comparison prepared by the all-in-one beaker method, where nanoscale Kirkendall diffusion was not applied, are shown in Figure 3. The product obtained by the drying process, shown in Supporting Information, Figure S2, was directly post-treated at 500 °C under air without the reduction process not to apply nanoscale Kirkendall effect. The SEM and TEM images shown in Figure 3a−c revealed aggregated $Fe_2O_3$ nanopowders with a dense structure. The high-resolution TEM image shown in Figure 3d revealed clear lattice fringes separated by 0.221 and 0.252 nm, which correspond to the (113) and (110) crystal planes of rhombohedral $\alpha$-$Fe_2O_3$, respectively. The SAED and XRD patterns shown in Figure 3e,f, respectively, revealed the formation of phase pure $Fe_2O_3$ nanopowders. Supporting Information, Figure S7, shows the morphologies of the $Fe_2O_3$ powders prepared from the solution without polystyrene (PS) that provides a good pathway for the reducing gas. The post-treatment of $Fe(acac)_3$-PAN composite powders without PS at 500 °C under air produced formless bulk iron oxide. The XRD pattern shown in Supporting Information, Figure S7d, revealed the mixed crystal structure of the $Fe_2O_3$ and $Fe_3O_4$ phases. The oxygen poor $Fe_3O_4$ phase was formed because oxygen gas did not penetrate the inside of the dried bulk material well. Therefore, PS played a key role in the preparation of $Fe_2O_3$ nanopowders with hollow and dense structures by the all-in-one beaker method as shown in Figure 1 and 2.

The electrochemical properties of the $Fe_2O_3$ hollow nanospheres for use in lithium-ion storage were compared to those of the nanopowders with a dense structure and the bulk material (Figure 4). The cyclic voltammogram (CV) curves of the $Fe_2O_3$ hollow nanospheres formed by the nanoscale


DOI: 10.1021/acsami.5b10278
ACS Appl. Mater. Interfaces 2016, 8, 3800−3809

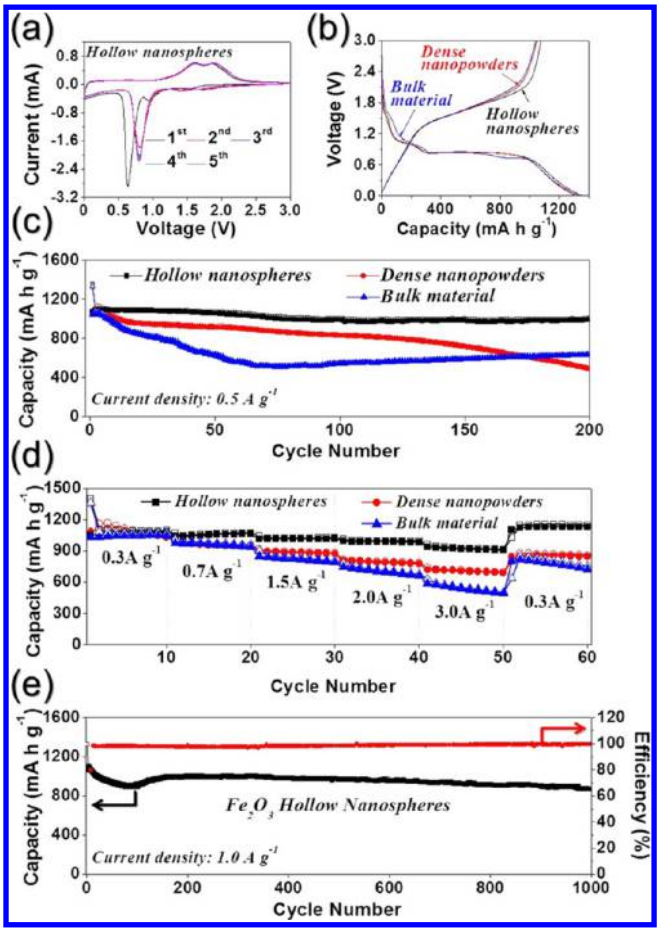


**Figure 4.** Electrochemical properties of the $Fe_2O_3$ hollow nanospheres and nanopowders with dense structure and bulk material: (a) CV curves of the $Fe_2O_3$ hollow nanospheres, (b) first charge−discharge curves at a current density of 0.5 A $g^{-1}$, (c) cycling performances at a current density of 0.5 A $g^{-1}$, (d) rate performances, and (e) long-term cycling performance and Coulombic efficiencies of the $Fe_2O_3$ hollow nanospheres at a current density of 1.0 A $g^{-1}$.

Kirkendall diffusion process for the first five cycles at a scan rate of 0.07 mV $s^{-1}$ over the voltage range of 0.001−3 V are shown in Figure 4a. The first reduction peak observed around 1.6 V in the first cathodic sweep corresponded to the initial lithium insertion into $Fe_2O_3$ and the reduction of iron from $Fe^{3+}$ to $Fe^{2+}$ without structural change. The second reduction peak observed at around 0.9 V was due to the phase transformation from hexagonal $Li_xFe_2O_3$ to cubic $Li_xFe_2O_3$.[37−40] The third obvious reduction peak observed at around 0.6 V corresponded to the reduction of iron from $Fe^{2+}$ to $Fe^0$ metal nanograins.[32,41−43] The two broad oxidation peaks observed at around 1.6 and 1.9 V in the anodic sweeps were attributed to the oxidation of $Fe^0$ to $Fe^{2+}$ and $Fe^{3+}$.[37−40] From the second cycle onward, the reduction peak shifted to a higher potential, around 0.8 V, because of the conversion of $Fe_2O_3$ into ultrafine nanocrystals during the first cycle.[44−46] The initial charge and discharge profiles of the three samples at a current density of 0.5 A $g^{-1}$ are shown in Figure 4b. The three samples had similar shapes and capacities in their initial charge and discharge profiles irrespective of their morphologies. The initial discharge and charge capacities of the $Fe_2O_3$ hollow nanospheres were 1356 and 1078 mA h $g^{-1}$, respectively, and their corresponding initial Coulombic efficiency was 79%. However, the cycling performances of the three samples were strongly affected by their morphologies, as shown in Figure 4c. The $Fe_2O_3$ hollow nanospheres showed good cycling performance over 200 cycles. The $Fe_2O_3$ nanopowders with a dense structure decreased during the first 20 cycles because of partial destruction of their structure during cycling. However, they later showed good cycling performance during the further 100 cycles. However, the discharge capacities of the iron oxide bulk material decreased continuously during the first 75 cycles, and then the capacities increased with increasing number of cycles because of the formation of a polymeric gel-like film on the active material as well as electrolyte decomposition. The discharge capacities of the $Fe_2O_3$ nanopowders with hollow and dense structures, and the bulk material after the 200th cycle were 1012, 498, and 637 mA h $g^{-1}$, respectively, and their capacity retentions calculated compared to the second cycles were 92, 45, and 59%, respectively. The rate performances of the three samples are shown in Figure 4d, in which the current density was increased stepwise from 0.3 to 3.0 A $g^{-1}$. The $Fe_2O_3$ hollow nanospheres showed superior rate performance compared with the nanopowders with dense structure and the bulk material. The final discharge capacities of the $Fe_2O_3$ hollow nanospheres at current densities of 0.3, 0.7, 1.5, 2.0, and 3.0 A $g^{-1}$ were 1095, 1074, 1027, 993, and 915 mA h $g^{-1}$, respectively. The discharge capacities decreased slightly with increasing current densities. In addition, the $Fe_2O_3$ hollow nanospheres showed good capacity recovery when the current density returns to 0.3 A $g^{-1}$ even after cycling at high current densities. The long-term cycling performance and Coulombic efficiencies of the $Fe_2O_3$ hollow nanospheres cycled at 1 A $g^{-1}$ are shown in Figure 4e. The $Fe_2O_3$ hollow nanospheres showed high Coulombic efficiencies above 99% from the second cycle onward. The initial discharge and charge capacities of the hollow nanospheres were 1327 and 1057 mA h $g^{-1}$, respectively. However, the initial capacity loss of the $Fe_2O_3$ hollow nanospheres was attributed to the partial destruction of the internal structure, the irreversible electrochemical decomposition of electrolyte, and the subsequent formation of a solid-electrolyte interphase (SEI) layer on the surface. Then, the slight decrease of the capacity after 400 cycles was due to the structure destruction owing to the stress forming by uptake of Li ion upon repeated further cycles. After 1000 cycles, the hollow nanospheres showed a high discharge capacity of 871 mA h $g^{-1}$ and their corresponding capacity retention calculated from the second cycle was 80%.

Electrochemical impedance spectroscopy (EIS) measurements before and after 1, 50, and 100 cycles were performed to reveal the superior electrochemical properties of the $Fe_2O_3$ hollow nanospheres compared with those of the nanopowders with dense structure and the bulk material. The Nyquist plots shown in Figure 5a−d display compressed semicircles in the medium frequency range, which describe the charge-transfer resistance ($R_{ct}$) of the electrode.[29,47,48] The aggregate-free $Fe_2O_3$ hollow nanospheres with a high surface area had the minimum charge-transfer resistance before cycling, as shown in Figure 5a. However, the bulk material with a low contact area with liquid electrolyte had the highest charge-transfer resistance before cycling. The charge-transfer resistances of the three samples decreased after the first cycle because of the formation of ultrafine nanocrystals during the first discharge and charge processes. The low charge-transfer resistance of the $Fe_2O_3$ hollow nanospheres with high structural stability was maintained during cycling for 100 cycles, as shown in Figure 5b. However, the charge-transfer resistances of the nano-


DOI: 10.1021/acsami.5b10278
ACS Appl. Mater. Interfaces 2016, 8, 3800−3809

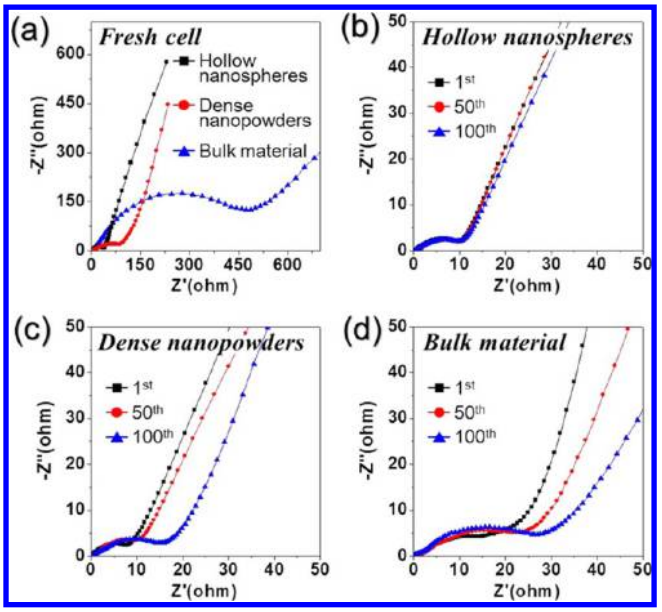


**Figure 5.** Nyquist plots of the $Fe_2O_3$ hollow nanospheres and nanopowders with dense structure and bulk material: (a) before cycling, (b) after cycling of the $Fe_2O_3$ hollow nanospheres, (c) after cycling of the $Fe_2O_3$ nanopowders with dense structure, and (d) after cycling of the bulk material.

powders with a dense structure and the bulk material increased with increasing number of cycles, as shown in Figure 5c,d. The morphological changes of the $Fe_2O_3$ hollow nanospheres and the $Fe_2O_3$ nanopowders with a dense structure obtained after 200 cycles were investigated by TEM in Supporting Information, Figure S8. The $Fe_2O_3$ hollow nanospheres maintained their overall morphology even after repeated lithium insertion and desertion processes. On the other hand, $Fe_2O_3$ nanopowders with a dense structure lost their original morphology and aggregated after cycling. The $Fe_2O_3$ hollow nanospheres having a high contact area with the liquid electrolyte and space for accommodating huge volume change during cycling showed excellent cycling and rate performance for lithium-ion storage (Supporting Information, Figure S9). Graphitic carbon coating layer formed by graphitization of amorphous carbon also improved the electrochemical properties of the $Fe_2O_3$ hollow nanospheres.

Furthermore, the strategy described in this study has generally applied to various metal oxide hollow nanospheres. We successfully synthesized many other metal oxide hollow nanospheres, such as NiO, $SnO_2$, and $Co_3O_4$ in Figure 6. The XRD patterns of the reduced samples at 500 °C for NiO and $Co_3O_4$ and at 400 °C for $SnO_2$ hollow nanospheres had peaks of metallic Ni, Co, and Sn, respectively, as shown in Supporting Information, Figure S10. The TEM images of the NiO, $SnO_2$, and $Co_3O_4$ nanopowders obtained after further oxidation process at 400 °C under air showed hollow structure as shown in Figure 6. The NiO, $SnO_2$, and $Co_3O_4$ hollow nanospheres were formed by the same formation mechanism of the $Fe_2O_3$ hollow nanospheres above studied. The cycling performances of the three samples at a current density of 1.0 A $g^{-1}$ are also shown in Figure 6. The initial discharge capacities of the NiO, $SnO_2$, and $Co_3O_4$ hollow nanospheres were 1074, 2098, and 1248 mA h $g^{-1}$, respectively, and their corresponding initial Coulombic efficiencies were 75, 42, and 76%, respectively. The discharge capacities of the NiO, $SnO_2$, and $Co_3O_4$ hollow nanospheres for the 250th cycles were 763, 845, and 1128 mA h $g^{-1}$, respectively, and their corresponding capacity retentions calculated from the second cycle were 94, 91, and 114%, respectively. The NiO, $SnO_2$, and $Co_3O_4$ hollow nanospheres

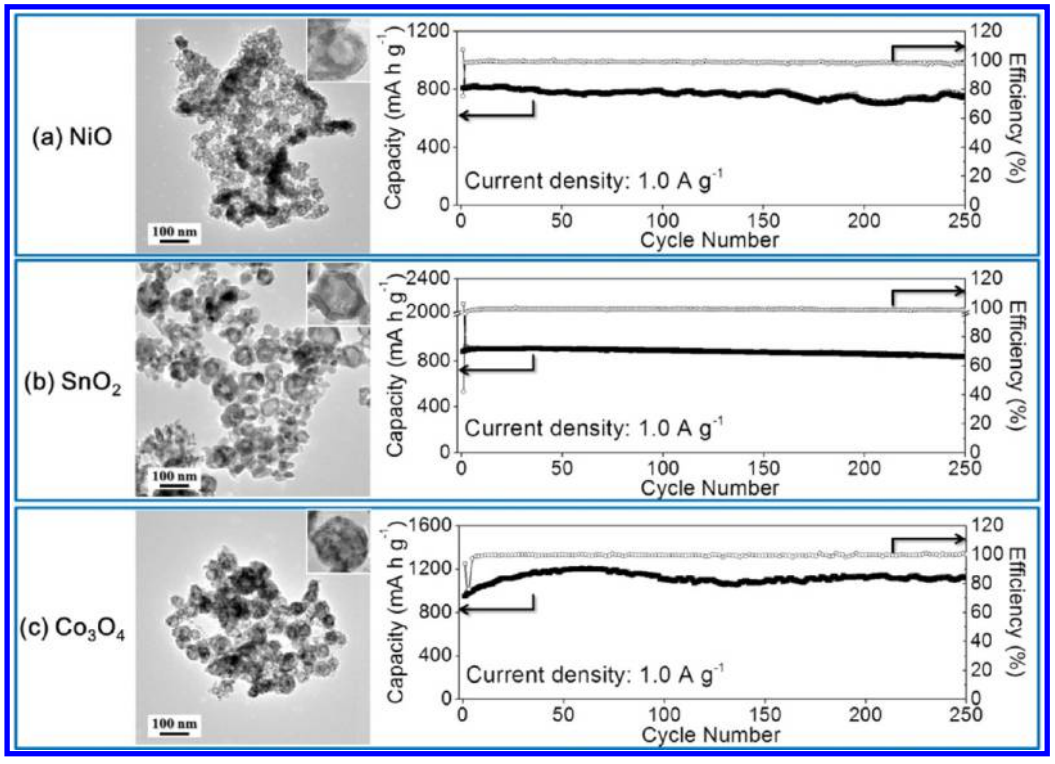


**Figure 6.** Morphologies and cycling performances at a current density of 1.0 A $g^{-1}$ for the (a) NiO, (b) $SnO_2$, and (c) $Co_3O_4$ hollow nanospheres formed by all-in-one beaker method.



DOI: 10.1021/acsami.5b10278
ACS Appl. Mater. Interfaces 2016, 8, 3800−3809

prepared by all-in-one beaker method had also excellent lithium-ion storage properties.

## CONCLUSIONS

In this study, a new process denoted as an "all-in-one beaker method" for aggregate-free metal oxide hollow nanospheres was studied. The viscous solution containing metal salt and organic polymers transformed into aggregate-free metal oxide hollow nanospheres in the glass beaker in a static furnace by simple drying and a thermal treatment process. The polyacrylonitrile (PAN) and polystyrene (PS) polymers played key roles in the formation of metal oxide hollow nanospheres. In particular, PS, which can be decomposed under a reducing atmosphere, enabled the formation of bulk C material decorated uniformly with the metal nanopowders. In addition, PAN, which is decomposed to carbon matrix, prevented the aggregation of metal nanopowders by surrounding each particle. The metal oxide hollow nanospheres formed by applying the nanoscale Kirkendall diffusion process had a regular morphology and excellent lithium-ion storage properties. The simple process developed in this study can be efficiently applied in the large-scale production of aggregate-free metal oxide nanospheres for various applications including lithium-ion batteries.

## ASSOCIATED CONTENT

### Supporting Information

The Supporting Information is available free of charge on the ACS Publications website at DOI: 10.1021/acsami.5b10278.

Schematic diagram for static three-step post-treatment process inside a glass beaker and photographs of the beakers containing the product obtained in each step; SEM image of the sample formed by drying process at 150 °C; TG curves of PAN and PS obtained in $N_2$ atmosphere; XRD patterns of the powders obtained by drying process, subsequent reduction process, and final oxidation process; TG analyses of the powders obtained after drying process, subsequent reduction process, and final oxidation process; Fe 2p XPS spectrum of the $Fe_2O_3$ hollow nanospheres obtained by all-in-one beaker method; morphologies and XRD pattern of the materials formed by all-in-one beaker method from the solution without polystyrene (PS); morphologies of the $Fe_2O_3$ hollow nanospheres and $Fe_2O_3$ nanopowders with a dense structure obtained after 200 cycles; schematic diagram for the mechanism of the lithium ion transport diffusion and storage in hollow nanosphere; XRD patterns of the metal-C composite powders obtained by reduction process and metal oxide hollow nanopowders obtained by further oxidation process during the all-in-one beaker method; TEM images of the $Fe_2O_3$ hollow nanopowders formed by all-in-one beaker method with different reduction temperatures; XRD patterns of the powders formed by all-in-one beaker method from the precursor solution without polystyrene (PS); TG analyses of the $Fe_2O_3$ nanopowders with dense structure obtained by direct oxidation process of the dried powders at 400 °C and bulk material prepared from the solution without PS; $N_2$ adsorption−desorption isotherms measured at 77 K for the $Fe_2O_3$ hollow nanospheres, $Fe_2O_3$ dense nanopowders, and bulk material (PDF)

## AUTHOR INFORMATION

### Corresponding Author

*E-mail: yckang@korea.ac.kr. Fax: (+82) 2-928-3584.

### Notes

The authors declare no competing financial interest.

## ACKNOWLEDGMENTS

This work was supported by the Energy Efficiency & Resources Core Technology Program of the Korea Institute of Energy Technology Evaluation and Planning (KETEP), granted financial resource from the Ministry of Trade, Industry & Energy, Republic of Korea (201320200000420).

## REFERENCES

(1) Gogotsi, Y. What Nano Can Do for Energy Storage. *ACS Nano* **2014**, *8*, 5369−5371.
(2) Fan, H. J.; Gösele, U.; Zacharias, M. Formation of Nanotubes and Hollow Nanoparticles Based on Kirkendall and Diffusion Processes: A Review. *Small* **2007**, *3*, 1660−1671.
(3) Lai, X.; Li, J.; Korgel, B. A.; Dong, Z.; Li, Z.; Su, F.; Du, J.; Wang, D. General Synthesis and Gas-Sensing Properties of Multiple-Shell Metal Oxide Hollow Microspheres. *Angew. Chem.* **2011**, *123*, 2790−2793.
(4) Li, D.; Qin, Q.; Duan, X.; Yang, J.; Guo, W.; Zheng, W. General One-Pot Template-Free Hydrothermal Method to Metal Oxide Hollow Spheres and Their Photocatalytic Activities and Lithium Storage Properties. *ACS Appl. Mater. Interfaces* **2013**, *5*, 9095−9100.
(5) Lou, X. W.; Archer, L. A.; Yang, Z. Hollow Micro-/Nanostructures: Synthesis and Applications. *Adv. Mater.* **2008**, *20*, 3987−4019.
(6) Niu, C.; Meng, J.; Han, C.; Zhao, K.; Yan, M.; Mai, L. $VO_2$ Nanowires Assembled into Hollow Microspheres for High-Rate and Long-Life Lithium Batteries. *Nano Lett.* **2014**, *14*, 2873−2878.
(7) Wang, B.; Chen, J. S.; Wu, H. B.; Wang, Z.; Lou, X. W. Quasiemulsion-Templated Formation of $\alpha$-$Fe_2O_3$ Hollow Spheres with Enhanced Lithium Storage Properties. *J. Am. Chem. Soc.* **2011**, *133*, 17146−17148.
(8) Wang, J.; Yang, N.; Tang, H.; Dong, Z.; Jin, Q.; Yang, M.; Kisailus, D.; Zhao, H.; Tang, Z.; Wang, D. Accurate Control of Multishelled $Co_3O_4$ Hollow Microspheres as High-Performance Anode Materials in Lithium-Ion Batteries. *Angew. Chem.* **2013**, *125*, 6545−6548.
(9) Cheng, F.; Liang, J.; Tao, Z.; Chen, J. Functional Materials for Rechargeable Batteries. *Adv. Mater.* **2011**, *23*, 1695−1715.
(10) Zhou, L.; Xu, H.; Zhang, H.; Yang, J.; Hartono, S. B.; Qian, K.; Zou, J.; Yu, C. Cheap and Scalable Synthesis of $\alpha$-$Fe_2O_3$ Multi-Shelled Hollow Spheres as High-Performance Anode Materials for Lithium Ion Batteries. *Chem. Commun.* **2013**, *49*, 8695−8697.
(11) Zhou, X.; Yin, Y. X.; Wan, L. J.; Guo, Y. G. A Robust Composite of $SnO_2$ Hollow Nanospheres Enwrapped by Graphene as a High-Capacity Anode Material for Lithium-Ion Batteries. *J. Mater. Chem.* **2012**, *22*, 17456−17459.
(12) An, K.; Hyeon, T. Synthesis and Biomedical Applications of Hollow Nanostructures. *Nano Today* **2009**, *4*, 359−373.
(13) Hu, J.; Chen, M.; Fang, X.; Wu, L. Fabrication and Application of Inorganic Hollow Spheres. *Chem. Soc. Rev.* **2011**, *40*, 5472−5491.
(14) Lai, X.; Halpert, J. E.; Wang, D. Recent Advances in Micro-/Nano-Structured Hollow Spheres for Energy Applications: From Simple to Complex Systems. *Energy Environ. Sci.* **2012**, *5*, 5604−5618.
(15) Lou, X. W.; Archer, L. A.; Yang, Z. Hollow Micro-/Nanostructures: Synthesis and Applications. *Adv. Mater.* **2008**, *20*, 3987−4019.
(16) Xia, X. H.; Tu, J. P.; Wang, X. L.; Gu, C. D.; Zhao, X. B. Mesoporous $Co_3O_4$ Monolayer Hollow-Sphere Array as Electrochemical Pseudocapacitor Material. *Chem. Commun.* **2011**, *47*, 5786−5788.


DOI: 10.1021/acsami.5b10278
*ACS Appl. Mater. Interfaces* 2016, 8, 3800−3809

(17) Zhang, Q.; Wang, W.; Goebl, J.; Yin, Y. Self-Templated Synthesis of Hollow Nanostructures. *Nano Today* **2009**, *4*, 494−507.
(18) Zhong, Y.; Su, L.; Yang, M.; Wei, J.; Zhou, Z. Rambutan-Like $FeCO_3$ Hollow Microspheres: Facile Preparation and Superior Lithium Storage Performances. *ACS Appl. Mater. Interfaces* **2013**, *5*, 11212−11217.
(19) Jana, S.; Chang, J. W.; Rioux, R. M. Synthesis and Modeling of Hollow Intermetallic Ni−Zn Nanoparticles Formed by the Kirkendall Effect. *Nano Lett.* **2013**, *13*, 3618−3625.
(20) Railsback, J. G.; Johnston-Peck, A. C.; Wang, J.; Tracy, J. B. Size-Dependent Nanoscale Kirkendall Effect during the Oxidation of Nickel Nanoparticles. *ACS Nano* **2010**, *4*, 1913−1920.
(21) Xiao, G.; Zeng, Y.; Jiang, Y.; Ning, J.; Zheng, W.; Liu, B.; Chen, X.; Zou, G.; Zou, B. Controlled Synthesis of Hollow $Cu_{2-x}Te$ Nanocrystals Based on the Kirkendall Effect and Their Enhanced CO Gas-Sensing Properties. *Small* **2013**, *9*, 793−799.
(22) Yin, Y.; Rioux, R. M.; Erdonmez, C. K.; Hughes, S.; Somorjai, G. A.; Alivisatos, A. P. Formation of Hollow Nanocrystals through the Nanoscale Kirkendall Effect. *Science* **2004**, *304*, 711−714.
(23) Cho, J. S.; Kang, Y. C. Nanofibers Comprising Yolk−Shell Sn@void@$SnO/SnO_2$ and Hollow $SnO/SnO_2$ and $SnO_2$ Nanospheres via the Kirkendall Diffusion Effect and Their Electrochemical Properties. *Small* **2015**, *11*, 4673−4681.
(24) Cho, J. S.; Hong, Y. J.; Lee, J. H.; Kang, Y. C. Design and Synthesis of Micron-Sized Spherical Aggregates Composed of Hollow $Fe_2O_3$ Nanospheres for Use in Lithium-Ion Batteries. *Nanoscale* **2015**, *7*, 8361−8367.
(25) Cho, J. S.; Hong, Y. J.; Kang, Y. C. Design and Synthesis of Bubble-Nanorod-Structured $Fe_2O_3$−Carbon Nanofibers as Advanced Anode Material for Li-Ion Batteries. *ACS Nano* **2015**, *9*, 4026−4035.
(26) Ai, Z.; Gao, Z.; Zhang, L.; He, W.; Yin, J. J. Core−Shell Structure Dependent Reactivity of $Fe@Fe_2O_3$ Nanowires on Aerobic Degradation of 4-Chlorophenol. *Environ. Sci. Technol.* **2013**, *47*, 5344−5352.
(27) Gupta, V.; Singh, S.; Rawat, K.; Bohidar, H.; Solanki, P. R. Cytotoxicity and Antimicrobial Activity of Transition Metal Oxide Nanoparticles. *Adv. Sci. Lett.* **2014**, *20*, 1650−1653.
(28) Jiang, L.; Gu, S.; Ding, Y.; Jiang, F.; Zhang, Z. Facile and Novel Electrochemical Preparation of a Graphene−Transition Metal Oxide Nanocomposite for Ultrasensitive Electrochemical Sensing of Acetaminophen and Phenacetin. *Nanoscale* **2014**, *6*, 207−214.
(29) Guo, B.; Wang, X.; Fulvio, P. F.; Chi, M.; Mahurin, S. M.; Sun, X. G.; Dai, S. Soft-Templated Mesoporous Carbon-Carbon Nanotube Composites for High Performance Lithium-Ion Batteries. *Adv. Mater.* **2011**, *23*, 4661−4666.
(30) Anasori, B.; Beidaghi, M.; Gogotsi, Y. Graphene−Transition Metal Ooxide Hhybrid Mmaterials. *Mater. Today* **2014**, *17*, 253−254.
(31) Sun, Z.; Liao, T.; Dou, Y.; Hwang, S. M.; Park, M. S.; Jiang, L.; Kim, J. H.; Dou, S. X. Generalized Self-Assembly of Scalable Two-Dimensional Transition Metal Oxide Nanosheets. *Nat. Commun.* **2014**, *5*, 3813.
(32) Choi, S. H.; Kang, Y. C. $Fe_3O_4$-Decorated Hollow Graphene Balls Prepared by Spray Pyrolysis Process for Ultrafast and Long Cycle-Life Lithium Ion Batteries. *Carbon* **2014**, *79*, 58−66.
(33) Yang, Z.; Zhou, X.; Jin, Z.; Liu, Z.; Nie, H.; Chen, X. a.; Huang, S. A Facile and General Approach for the Direct Fabrication of 3D, Vertically Aligned Carbon Nanotube Array/Transition Metal Oxide Composites as Non-Pt Catalysts for Oxygen Reduction Reactions. *Adv. Mater.* **2014**, *26*, 3156−3161.
(34) Yuan, C.; Wu, H. B.; Xie, Y.; Lou, X. W. Mixed Transition-Metal Oxides: Design, Synthesis, and Energy-Related Applications. *Angew. Chem., Int. Ed.* **2014**, *53*, 1488−1504.
(35) Er, D.; Li, J.; Naguib, M.; Gogotsi, Y.; Shenoy, V. B. $Ti_3C_2$ MXene as a High Capacity Electrode Material for Metal (Li, Na, K, Ca) Ion Batteries. *ACS Appl. Mater. Interfaces* **2014**, *6*, 11173−11179.
(36) Yang, P.; Ding, Y.; Lin, Z.; Chen, Z.; Li, Y.; Qiang, P.; Ebrahimi, M.; Mai, W.; Wong, C. P.; Wang, Z. L. Low-Cost High-Performance Solid-State Asymmetric Supercapacitors Based on $MnO_2$ Nanowires and $Fe_2O_3$ Nanotubes. *Nano Lett.* **2014**, *14*, 731−736.
(37) Gao, G.; Yu, L.; Wu, H. B.; Lou, X. W. D. Hierarchical Tubular Structures Constructed by Carbon-coated $\alpha$-$Fe_2O_3$ Nanorods for Highly Reversible Lithium Storage. *Small* **2014**, *10*, 1741−1745.
(38) Son, M. Y.; Hong, Y. J.; Lee, J. K.; Kang, Y. C. One-Pot Synthesis of $Fe_2O_3$ Yolk−Shell Particles with Two, Three, and Four Shells for Application as an Anode Material in Lithium-Ion Batteries. *Nanoscale* **2013**, *5*, 11592−11597.
(39) Zhang, W. M.; Wu, X. L.; Hu, J. S.; Guo, Y. G.; Wan, L. J. Carbon Coated $Fe_3O_4$ Nanospindles as a Superior Anode Material for Lithium-Ion Batteries. *Adv. Funct. Mater.* **2008**, *18*, 3941−3946.
(40) Zhao, Y.; Li, J.; Ding, Y.; Guan, L. Single-Walled Carbon Nanohorns Coated with $Fe_2O_3$ as a Superior Anode Material for Lithium Ion Batteries. *Chem. Commun.* **2011**, *47*, 7416−7418.
(41) Xu, X.; Cao, R.; Jeong, S.; Cho, J. Spindle-Like Mesoporous $\alpha$-$Fe_2O_3$ Anode Material Prepared from MOF Template for High-Rate Lithium Batteries. *Nano Lett.* **2012**, *12*, 4988−4991.
(42) Ye, J.; Zhang, J.; Wang, F.; Su, Q.; Du, G. One-Pot Synthesis of $Fe_2O_3$/Graphene and Its Lithium-Storage Performance. *Electrochim. Acta* **2013**, *113*, 212−217.
(43) Zhu, X.; Zhu, Y.; Murali, S.; Stoller, M. D.; Ruoff, R. S. Nanostructured Reduced Graphene Oxide/$Fe_2O_3$ Composite as a High-Performance Anode Material for Lithium Ion Batteries. *ACS Nano* **2011**, *5*, 3333−3338.
(44) Chen, J.; Xu, L. N.; Li, W. Y.; Gou, X. L. $\alpha$-$Fe_2O_3$ Nanotubes in Gas Sensor and Lithium-Ion Battery Applications. *Adv. Mater.* **2005**, *17*, 582−586.
(45) Cherian, C. T.; Sundaramurthy, J.; Kalaivani, M.; Ragupathy, P.; Kumar, P. S.; Thavasi, V.; Reddy, M.; Sow, C. H.; Mhaisalkar, S. G.; Ramakrishna, S.; Chowdari, B. V. R. Electrospun $\alpha$-$Fe_2O_3$ Nanorods as a Stable, High Capacity Anode Material for Li-Ion Batteries. *J. Mater. Chem.* **2012**, *22*, 12198−12204.
(46) Han, F.; Li, D.; Li, W. C.; Lei, C.; Sun, Q.; Lu, A. H. Nanoengineered Polypyrrole-Coated $Fe_2O_3$@C Multifunctional Composites with an Improved Cycle Stability as Lithium-Ion Anodes. *Adv. Funct. Mater.* **2013**, *23*, 1692−1700.
(47) Hong, Y. J.; Son, M. Y.; Kang, Y. C. One-Pot Facile Synthesis of Double-Shelled $SnO_2$ Yolk-Shell-Structured Powders by Continuous Process as Anode Materials for Li-ion Batteries. *Adv. Mater.* **2013**, *25*, 2279−2283.
(48) Li, N.; Liu, G.; Zhen, C.; Li, F.; Zhang, L.; Cheng, H. M. Battery Performance and Photocatalytic Activity of Mesoporous Anatase $TiO_2$ Nanospheres/Graphene Composites by Template-Free Self-Assembly. *Adv. Funct. Mater.* **2011**, *21*, 1717−1722.


DOI: 10.1021/acsami.5b10278
*ACS Appl. Mater. Interfaces* 2016, 8, 3800−3809